36C.0 COMBINING IN-SITU AND EX-SITU CHARACTERIZATION TO UNDERSTAND CRYSTALLOGRAPHIC TEXTURE DEVELOPMENT IN METAL ADDITIVE MANUFACTURING

Jonah Klemm-Toole (Mines)
Faculty: Amy Clarke (Mines)
Industrial Mentor: TBD

This project was initiated in Spring 2019 and is supported by an Office of Naval Research (ONR) Multidisciplinary University Research Initiative (MURI). The research performed during this project will serve as the contribution of Jonah Klemm-Toole as a Post-Doctoral Fellow in CANFSA.

36C.1 Project Overview and Industrial Relevance

The emergence of metal additive manufacturing (MAM) has unlocked the possibility to create complex geometries with location and orientation specific properties. The vast parameter space available in MAM enables the creation of unique microstructures that are not possible with conventional processing. However, as MAM is not a mature technology, there is not a full understanding of processing-microstructure-property relationships. Recent reviews by the Federal Aviation Administration (FAA) and National Institute for Standards and Technology [36C.1] have identified anisotropic mechanical properties as a characteristic of MAM that hinders broad implementation. **Figure 36C.1** illustrates the expected application of MAM as the technology matures [36C.2]. In order to apply MAM to high value, failure critical components such as gas turbine airfoils, the origins of anisotropic mechanical properties in MAM must be investigated further. Crystallographic texture, or non-random grain orientations, is expected to be a major contributor to anisotropic mechanical properties observed in MAM. In this project, we aim to combine *in-situ* characterization, e.g. X-ray radiography during laser melting to simulate laser-based MAM, with *ex-situ* characterization, such as scanning electron microscopy (SEM) and electron backscatter diffraction (EBSD), to better understand crystallographic texture development in MAM. It is expected that the outcome of this project will contribute to a deeper understanding of processing-microstructure-property relationships and enable the broader implementation of MAM.

36C.2 Previous Work – Literature Review

The majority of literature related to crystallographic texture in MAM focuses on the observance and/or control of a ⟨100⟩ fiber texture for Ni-based alloys and other cubic metals, where a large fraction of the grains (more than random) are oriented with a ⟨100⟩ direction parallel to the build direction [36C.3]. Although one ⟨100⟩ direction of a given grain may be parallel to the build direction, the other axes of the grain are generally random with respect to the MAM build. Dendrites in cubic metals typically grow along ⟨100⟩ directions, and the columnar dendritic solidification often observed in MAM results in a large fraction of grains having a ⟨100⟩ direction parallel to the build direction. The ⟨100⟩ fiber texture can be suppressed if the columnar to equiaxed transition (CET) is induced, such that random grain orientations grow, as illustrated in **Figure 36C.2**.

36C.3 Recent Progress

36C.3.1 Experimental Design

The AM simulator at the Advanced Photon Source (APS) at Argonne National Laboratory was used to obtain *in-situ* radiography during laser melting and subsequent solidification to simulate laser-based MAM. The objectives of experiments at the APS were to investigate the effects of 1) spot and raster melting strategies, 2) laser power, 3) single crystal substrate orientation, and 4) composition on the occurrence of the CET during simulated MAM. **Figure 36C.3** shows a schematic of the AM simulator at the 32-ID beamline of the APS [36C.4]. **Table 36C.1** summarizes the specimens evaluated at the APS thus far.

36C.3.2 *Ex-Situ* EBSD

A representative set of superimposed EBSD inverse pole figure (IPF) and image quality (IQ) maps for the Ni-1.9Mo-6.6Al (wt pct) alloy with a ⟨111⟩ direction parallel to the build direction (referred to as Ni-1.9Mo-6.6Al -111), including the full range of laser powers investigated is shown in **Figure 36C.4**. The coloring of the IPF maps corresponds to the crystallographic orientations parallel to the build direction. With decreasing laser power, more new grain orientations are observed in the EBSD maps. The traces of $\langle 100 \rangle$ directions are schematically shown in the IPF + IQ maps to indicate the orientations of dendritic growth. The dendrite growth orientations are used to estimate dendrite growth velocity from the motion of the solid-liquid interface determined from radiography.

36C.3.3 *In-Situ* Radiography

Radiography obtained during laser melting and solidification was analyzed to measure the velocity of the solid-liquid interface. **Figure 36C.5a** shows a radiograph of a Ni-1.9Mo-6.6Al -111 alloy sample during solidification. The white arrows point to the location of the solid-liquid interface at the beginning of solidification, and the red arrows point to the location of the interface at a later time. Radiography images were processed by dividing all images by the first image using ImageJ to minimize artifacts and highlight the solid-liquid interface. By tracking the progression of the solid-liquid interface and accounting for the time between images, the solidification velocity was measured. The traces of $\langle 100 \rangle$ directions were used to orient the velocity measurements, such that they are parallel to the dendrite growth directions. **Figure 36C.5b** shows a plot of solidification velocity, measured along a $\langle 100 \rangle$ direction, as a function of position from the edge of the melt pool to the center for Ni-1.9Mo-6.6Al -111 samples melted with the full range of laser powers investigated. Solidification velocity is observed to increase from the bottom to the top of the melt pool. Furthermore, the lower laser power conditions are observed to have higher maximum solidification velocities. Both trends of increased solidification velocity correlate with new grain nucleation, *i.e.* the CET.

36C.3.4 Heat Transfer Modeling

The spot and raster experiments were modeled using conduction heat transfer equations, assuming a semi-infinite solid to obtain rough estimates of thermal gradients during solidification. Spot melting was modeled using **Equation 36C.1**:

$$T - T_0 = \frac{\beta Q}{\rho C (4\pi\alpha t)^{1.5}} e^{\left(\frac{R^2}{4\alpha t}\right)} \qquad [36C.1]$$

where T is the temperature at a given place and time; T_0 is the starting temperature; β is the efficiency of energy absorption from the laser; Q is the total amount of heat delivered by the laser; ρ is the density of the solid; C is the heat capacity of the solid; α is thermal diffusivity of the solid; t is time; and R is the radial distance from the laser [36C.5]. Raster melting was modeled using **Equation 36C.2**:

$$T - T_0 = \frac{\beta P}{2\pi k R} e^{\left(-\frac{v(R+x)}{2\alpha}\right)} \qquad [36C.2]$$

where T, T_0, β, R, α have the same meanings as in **Equation 36C.1**; k is thermal conductivity of the solid; v is raster velocity; and x is the distance from the laser in the travel direction [36C.6]. Material properties for IN718 were used for the calculations; 7451 kg/m^3 was used for ρ, 600 J/(kg K) was used for C; 5.95 × 10^{-6} m^2/s was used for α; and 26.6 W/(m K) was used for k [36C.7]. Values for β were adjusted, such that the size of the melt pool predicted by the model matches the experimental result. A comparison of calculated solidification velocity to measured velocity for spot melts on Ni-1.9Mo-6.6Al -111 are shown in **Figure 36C.6a**. In general, the model predicts higher velocities than measured experimentally, although the observed trends of higher velocities at the end of solidification and with lower laser powers are predicted. A comparison of model predictions with experimental results for a Ni-22.2Mo-2.8Al-110 sample raster melted with a power of 156 W and a speed of 0.5 m/s is shown in **Figure 36C.6b**. In general, the model for raster melting more closely predicts experimental results compared to the spot melting model. More sophisticated heat transfer models that include fluid flow and can account for actual sample geometries using the FLOW-3D software package are being pursued.

36C.3.5 Columnar to Equiaxed Transition (CET) Modeling

A columnar to equiaxed transition (CET) model was investigated to better understand the role of solidification conditions and alloy composition on the appearance of new grain orientations. Michael Haines from the University of Tennessee Knoxville, who is a participant in the MURI project, performed the modeling. The model used is shown in **Equation 36C.3:**

$$G = \frac{1}{n+1} \sqrt[3]{\frac{-4\pi N_0}{3\ln(1-\emptyset)}} \Delta T \left(1 - \frac{\Delta T_n^{n+1}}{\Delta T^{n+1}}\right) \quad [36C.3]$$

where G is thermal gradient; n is a constant that depends on composition; N_0 is the nucleation site density; $\emptyset$ is the fraction of equiaxed grains; ΔT is the total undercooling in the liquid; and ΔT_n is the undercooling required for nucleation [36C.8]. The model essentially calculates how fast new random grains can grow in the liquid ahead of the advancing columnar dendritic front as a function of thermal gradient, solidification velocity, and solute partitioning to the liquid, as shown schematically in **Figure 36C.7a**. Representative results combining the observation of new grains from EBSD, solidification velocity measurements from radiography, thermal gradient calculations from heat transfer models, and CET model results are shown in **Figure 36C.7b** and **c** for Ni-1.9Mo-6.6Al -111 and Ni-22.2Mo-2.8Al-110, respectively. The dashed lines represent the thermal gradients and solidification velocities during solidification predicted by heat transfer models. The solid overlays to the dashed lines indicate the range of velocities measured experimentally. The symbols note when new grains were observed with EBSD. In general, the combination of CET and heat transfer models do not predict experimental results, *i.e.* the CET is observed when the models still predict columnar growth. The nucleation site density in the model, N_0, which must be calibrated to experimental results, was calibrated to a different set of experiments for the first iteration of the model. Better estimates of thermal gradients for the APS experiments and *ex-situ* microstructure characterization must be obtained in order to calibrate N_0 to the results presented here. Although the models do not yet predict experimental results, it appears that changes in solidification conditions from changing laser power have a greater effect on the occurrence of the CET than alloy composition or substrate orientation. **Table 36C.2** summarizes the experimental observation of CET in all conditions evaluated thus far.

36C.4 Plans for Next Reporting Period

Work to follow in the next reporting period includes:

- EBSD of remaining conditions noted in **Table 36C.2**;
- Heat transfer simulations using FLOW-3D to get better estimates of thermal gradients;
- Calibrate CET model using EBSD and heat transfer simulations;
- Preparation of journal articles.

36C.5 References

[36C.1] M. Seifi, M. Gorelik, J. Walker, N. Hrabe, N. Shamsaei, S. Daniewicz, J.J. Lewandowski, Progress towards metal additive manufacturing standardization to support qualification and standardization, JOM. 69:3 (2017) 439-455.

[36C.2] M. Gorelik, Additive manufacturing in the context of structural integrity, International Journal of Fatigue. 94 (2017) 168-177.

[36C.3] R.R. Dehoff, M.M. Kirka, W.J. Sames, H. Bilheux, A.S. Tremsin, L.E. Lowe, S.S. Babu, Site specific control of crystallographic grain orientation through electron beam additive manufacturing, Materials Science and Technology. 31:8 (2015) 931-938.

[36C.4] C. Zhao, K. Fezzaa, R.W. Cunningham, H. Wen, F. De Carlo, L. Chen, A.D. Rollett, T. Sun, Real-time monitoring of laser powder bed fusion process using high-speed X-ray imaging and diffraction, Scientific Reports. 7:3602 (2017) 1-11.

[36C.5] V.A. Karkhin, Thermal Processes in Welding, Second ed, Springer Nature, 2015, p. 158.

[36C.6] P. Promoppatum, S.C. Yao, P.C. Pistorius, A.D. Rollett, A comprehensive comparison of the analytical and numerical prediction of the thermal history and solidification microstructure of inconel 718 products made by laser powder-bed fusion, Engineering. 3 (2017) 685-694.

[36C.7] A. Plotowski, M.M. Kirka, S.S. Babu, Verification and validation of a rapid heat transfer calculation methodology for transient melt pool solidification conditions in powder bed metal additive manufacturing, Additive Manufacturing. 18 (2017) 256-268.

[36C.8] M. Haines, A. Plotowski, C.L. Frederick, E.J. Schwalbach, S.S. Babu, A sensitivity analysis of the columnar-to-equiaxed transition for Ni-based superalloys in electron beam additive manufacturing, Computational Materials Science. 155 (2018) 340-349.

36C.6 Figures and Tables

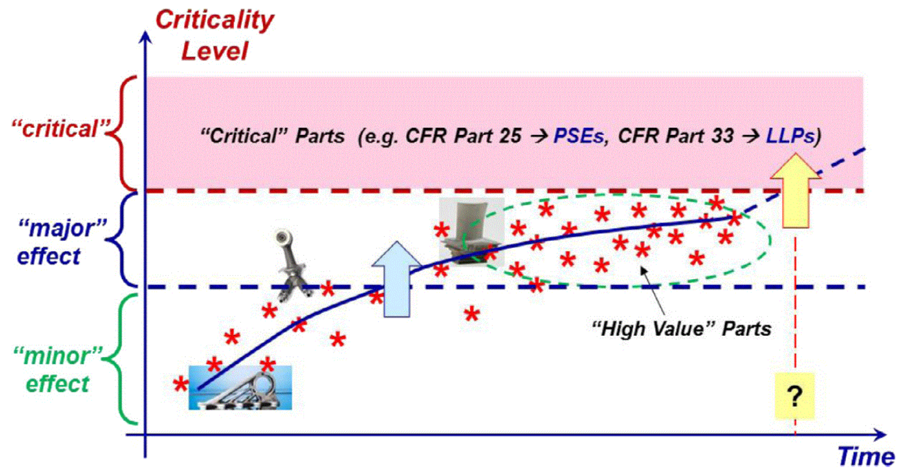

Figure 36C.1: Projected maturity of AM technology. With a better understanding of processing-microstructure-mechanical property relationships developed over time, AM can be applied to high value, failure critical components such as gas turbine airfoil components [36C.2].

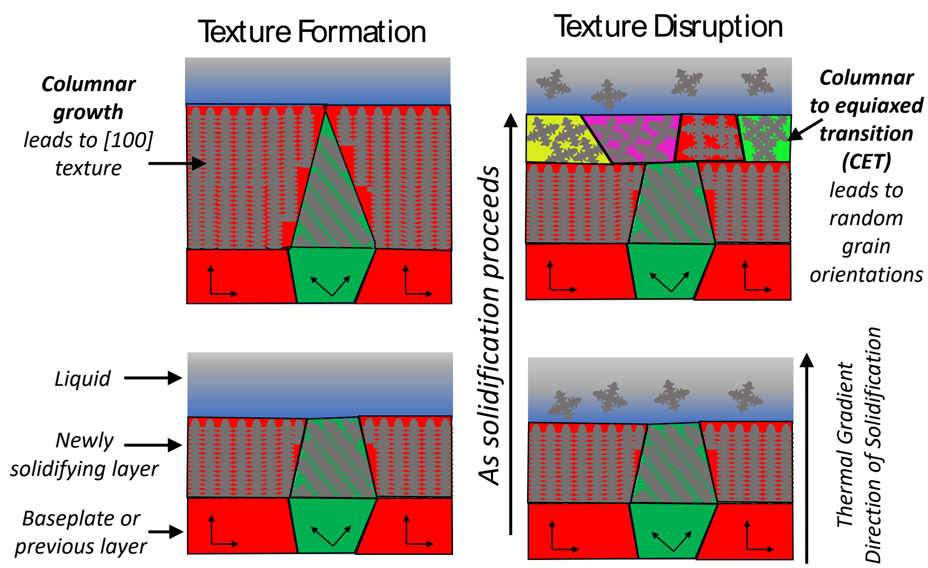

Figure 36C.2: Schematic of crystallographic texture development and disruption during solidification in MAM. Texture development occurs by favorably oriented grains ([100] directions parallel to the build direction) growing at the expense of other grain orientations. Texture disruption occurs by random grain orientations growing ahead of the advancing columnar dendritic front, leading to the columnar to equiaxed transition (CET).

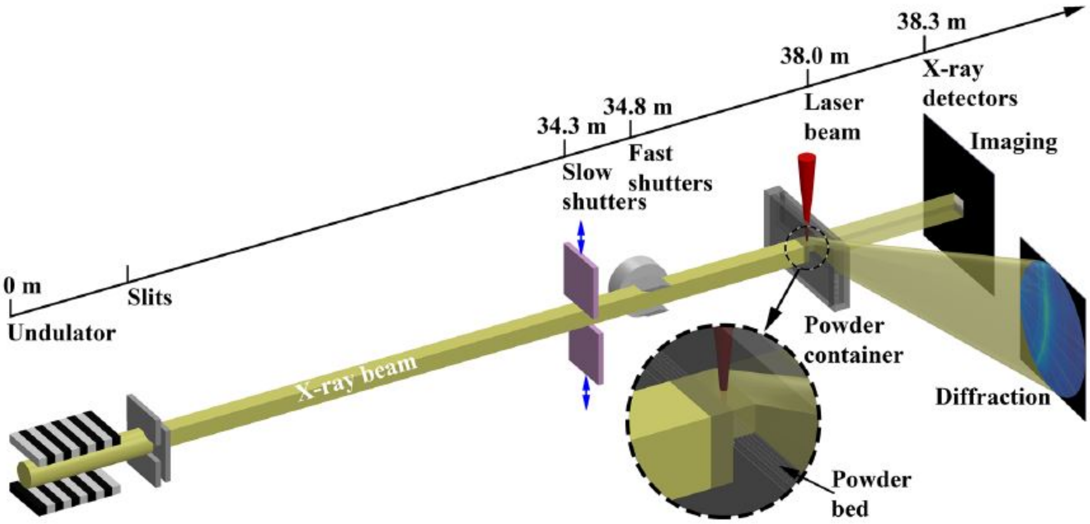

Figure 36C.3: Schematic of the AM simulator at Sector 32 of the APS. Synchrotron X-ray radiography and diffraction can be obtained during laser melting and solidification of bulk and/or powder samples [36C.4].

Table 36C.1: Experimental Conditions Evaluated

Composition [wt %]	Ni-22.2Mo-2.8Al		Ni-1.9Mo-6.6Al	
Orientation of Build Direction	⟨100⟩	⟨110⟩	⟨110⟩	⟨111⟩
Orientation of Normal Direction	⟨100⟩	⟨100⟩	⟨110⟩	⟨110⟩
Spot Melting Parameters	106, 156, 208, or 260 W for 1 ms			
Raster Melting Parameters	156 W at 0.5 m/s			

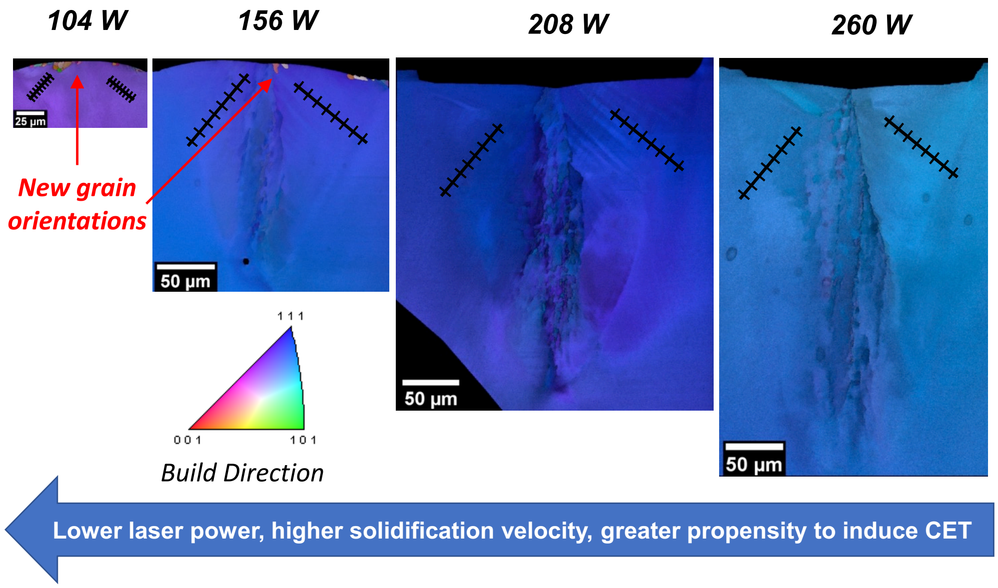

Figure 36C.4: EBSD IPF + IQ maps of the Ni-1.9Mo-6.6Al alloy with a ⟨111⟩ direction parallel to the build direction (referred to as Ni-1.9Mo-6.6Al -111) laser melted with 106, 156, 208, and 260 W for 1 ms. The coloring of the IPF maps indicate the crystallographic orientation parallel to the build direction. The two lower power conditions (106 and 156 W) show new grain orientations at the tops of the melt pools. The presence of new grain orientations correlates with higher solidification velocities, which is expected to increase the propensity to induce the CET.

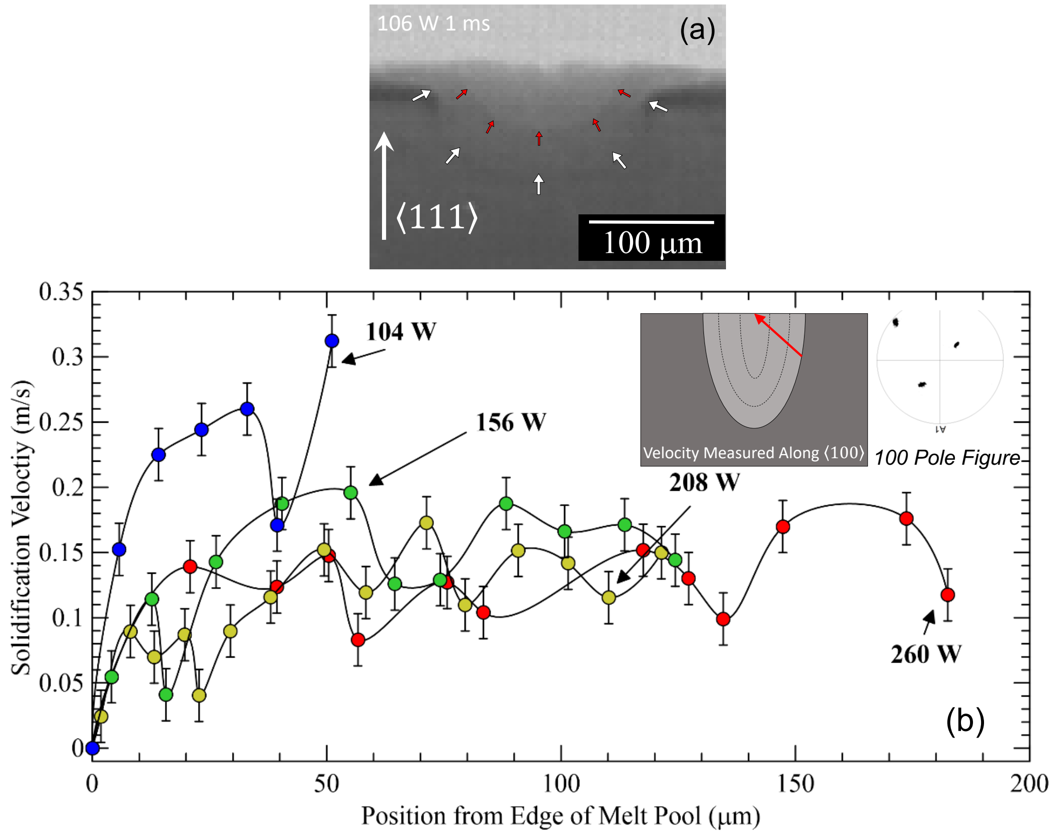

Figure 36C.5: (a) Example radiograph of Ni-1.9Mo-6.6Al -111 laser melted at 106 W for 1 ms. White arrows indicate the position of the solid-liquid interface at the beginning of solidification. Red arrows point to the position of the solid-liquid interface at a later time. (b) Measurements of the velocity of the solid liquid interface, measured along a ⟨100⟩ direction, as a function of position from the bottom of the melt pool made from radiography images. Solidification velocity is observed to increase from the bottom to the top of the melt pool. Higher solidification velocities are observed at the end of solidification and with lower power conditions.

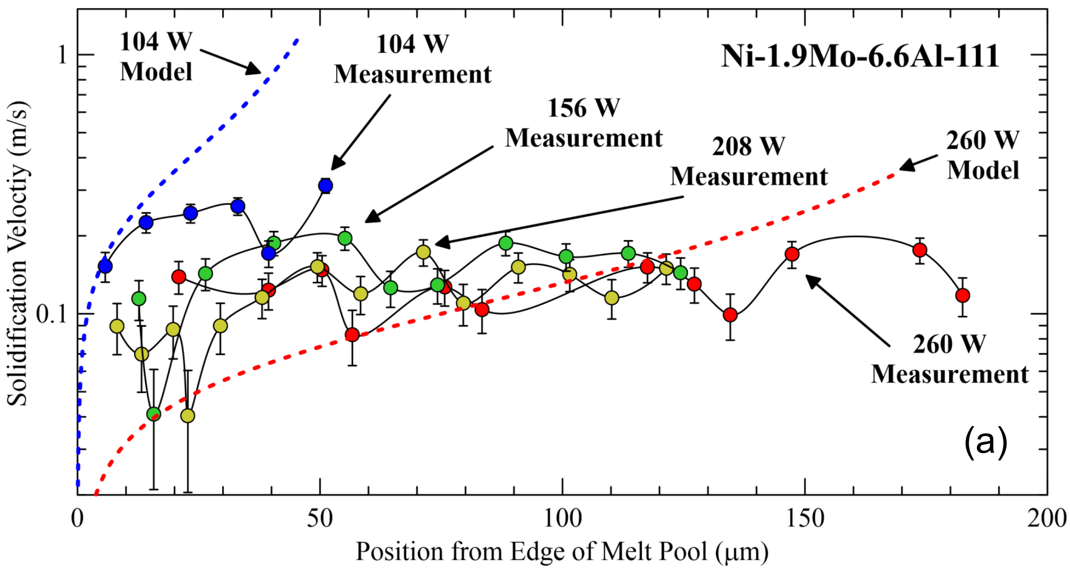

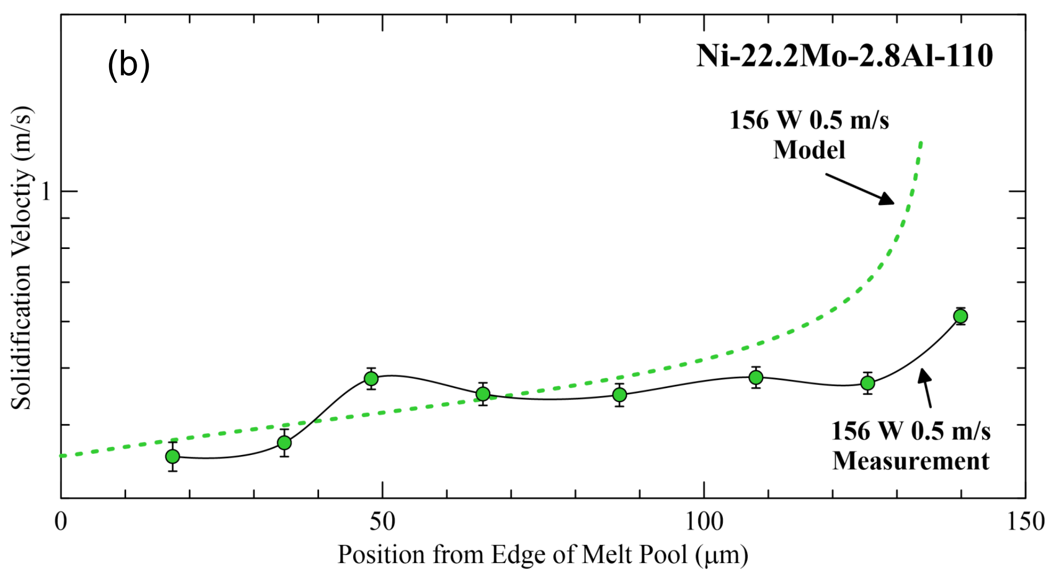

Figure 36C.6: Comparisons of heat transfer predictions and measurements of solidification velocity for (a) Ni-1.9Mo-6.6Al -111 spot melted with the full range of powers investigated, and (b) Ni-22.2Mo-2.8Al -110 raster melted with a power of 156 W at a speed of 0.5 m/s. In general, the heat transfer models over predict solidification velocity, but qualitatively predict that velocity increases from the bottom to the top of the melt pool and with lower laser powers. The model for raster melting predicts velocities that are closer to measurements compared to the model for spot melting.

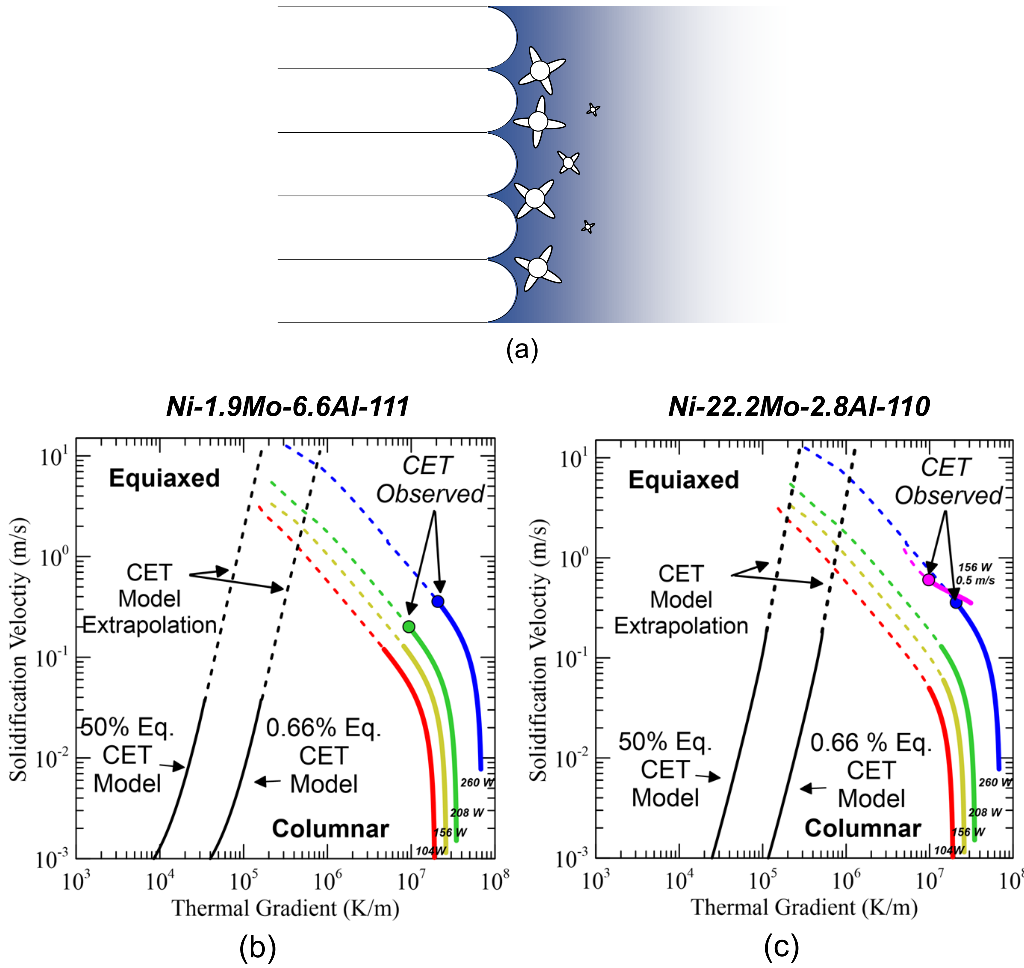

Figure 36C.7: (a) Schematic illustration of the CET where random grain orientations grow in the liquid ahead of the advancing columnar dendritic front. (b) and (c) Comparison of heat transfer calculations, measured solidification velocities from radiography, new grain orientation observations from EBSD, and CET model predictions for Ni-1.9Mo-6.6Al -111 and Ni-22.2Mo-2.8Al -110, respectively. The dashed lines show predicted solidification velocity and thermal gradient from the beginning to end of solidification predicted by heat transfer models. The solid overlays show the range of solidification velocity measured from radiography. The symbols indicate where new grain orientations are observed using EBSD. The black lines show where the CET is expected to occur. In general, the heat transfer and CET models to not predict experimental results. More sophisticated heat transfer modeling and calibration of the CET models are needed.

Table 36C.2: Summary of Experimental Conditions that Exhibit Columnar to Equiaxed Transition

CET Observed in EBSD?	**Spot**				**Raster**
Alloy – Build Direction	**106 W 1 ms**	**156 W 1 ms**	**208 W 1 ms**	**260 W 1 ms**	**156 W 0.5 m/s**
Ni-22.2Mo-2.8Al-100	Y	Y	Y	Pending	Pending
Ni-22.2Mo-2.8Al-110	Y	N	N	N	Y
Ni-1.9Mo-6.6Al-110	Y	Y	Y	Pending	Pending
Ni-1.9Mo-6.6Al-111	Y	Y	N	N	Pending